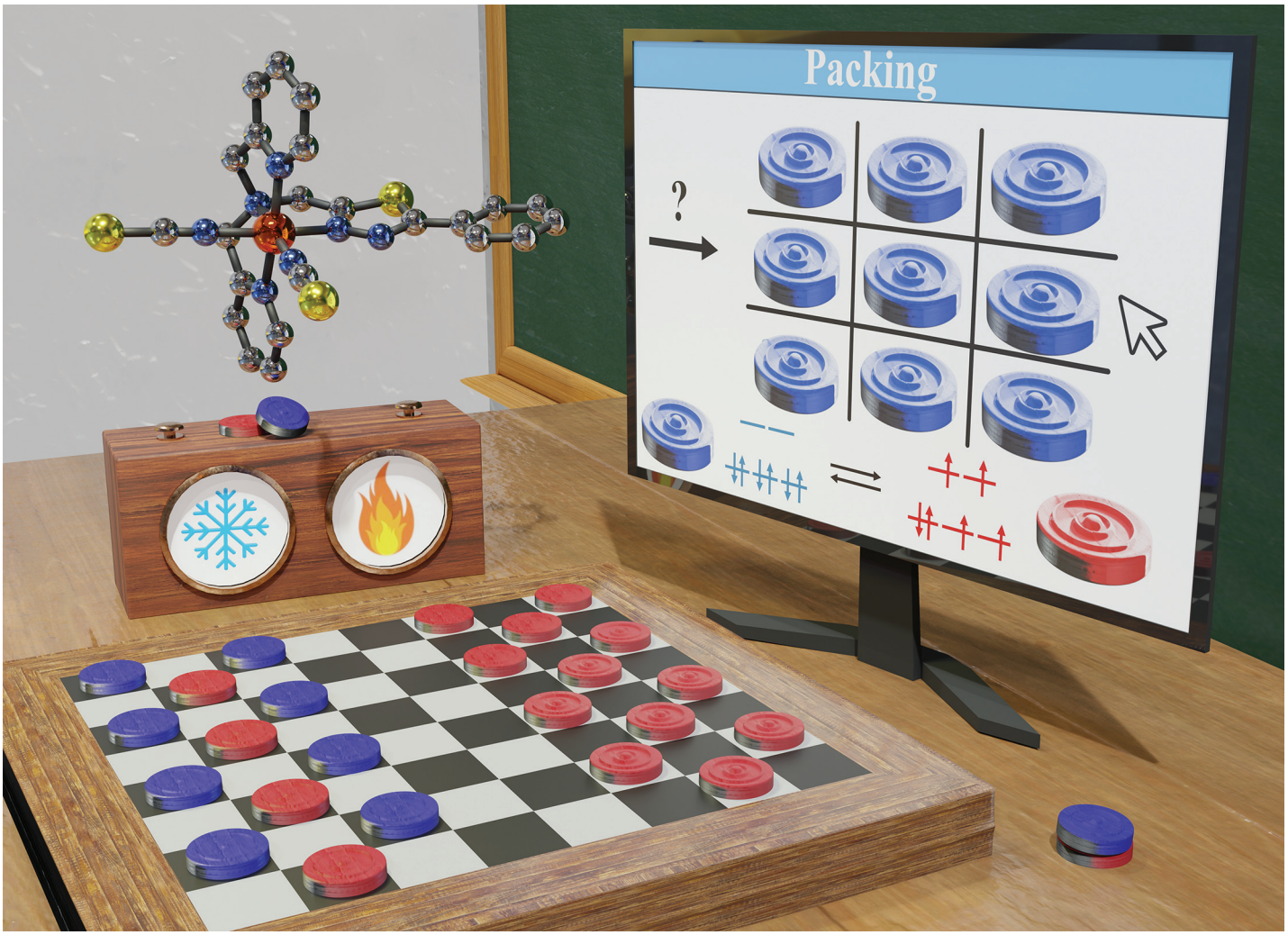

Showcasing research from Professor Eva Rentschler's laboratory, Chemistry Department, Johannes Gutenberg University Mainz, Germany.

Sub lattice driven spin state ordering and coordination elasticity in Fe(II) 1,3,4-thiadiazole complexes

A sublattice-driven spin crossover in the iron(II) complex $[Fe(LPh\text{-}TDA)(NCS)_2]\cdot H_2O$ was investigated by temperature-dependent XRD, SQUID magnetometry, and Mössbauer spectroscopy. Of the two crystallographically independent Fe(II) centers, only one undergoes a thermally induced spin transition, yielding a mixed spin-state lattice. Low-temperature light irradiation enables access to a hidden fully high-spin state *via* LIESST, whereas the fully low-spin state is inaccessible. This behaviour is explained by crystal packing effects and coordination elasticity, supported by DFT calculations.

Image reproduced by permission of Jens-Georg Becker and Eva Rentschler from *Dalton Trans.*, 2026, **55**, 2833.

As featured in:

See Eva Rentschler *et al.*, *Dalton Trans.*, 2026, **55**, 2833.

ROYAL SOCIETY OF CHEMISTRY

rsc.li/dalton

Registered charity number: 207890

Dalton Transactions

ROYAL SOCIETY OF CHEMISTRY

PAPER

View Article Online
View Journal | View Issue

Cite this: *Dalton Trans.*, 2026, **55**, 2833

Sub lattice driven spin state ordering and coordination elasticity in Fe(II) 1,3,4-thiadiazole complexes

Jens-Georg Becker, [a] Sriram Sundaresan, [a,b] Tim Hochdörffer, [c] Juliusz A. Wolny, [c] Luca M. Carrella, [a] Volker Schünemann [c] and Eva Rentschler *[a]

Understanding the role of co-ligand identity, governing spin-state energetics in many Fe(II) complexes, is essential for designing responsive spin-crossover materials. We report the synthesis of an unsymmetrical bis(pyridin-2-ylmethyl)glycyl benzohydrazide-derived ligand, 1-(5-phenyl-1,3,4-thiadiazol-2-yl)-*N*,*N*-bis(pyridin-2-ylmethyl)methanamine ($L^{Ph\text{-}TDA}$), and its corresponding complexes $[Fe(L^{Ph\text{-}TDA})(NCE)_2]\cdot H_2O$ (E = S (**C1**), Se (**C2**), BH_3 (**C3**)). While the ligand-field strength gradient ranges from weak (NCS^-) to strong ($NCBH_3^-$), the SCO behaviour of the resulting complexes does not reflect this. Variable-temperature single-crystal X-ray diffraction, SQUID magnetometry and ^{57}Fe Mössbauer spectroscopy show that there is packing-induced sublattice spin-state ordering for **C1**, which has two distinct Fe(II) sites. Of these sites, only one transitions to the low-spin state in two complexes, while the second remains locked in the high-spin (HS) state. **C2** remains high-spin throughout the entire temperature range, whereas **C3** exhibits a complete, one-step SCO with $T_{1/2}$ = 153 K. Density functional theory (DFT) calculations help to quantify the energetic origin of the ordered LS–HS configuration in **C1** and demonstrate that intermolecular packing effects override intrinsic ligand-field trends. These results highlight the dominant role of solid-state organization in dictating SCO behavior, even in systems engineered to isolate co-ligand electronic effects.

Received 5th December 2025,
Accepted 27th January 2026

DOI: 10.1039/d5dt02912k

rsc.li/dalton

Introduction

Molecular materials often exhibit fascinating ordering phenomena, in which the arrangement of molecules within a crystal lattice dictates their electronic, magnetic, and optical properties.[1–10] These effects are particularly pronounced in molecular solids, where the balance between intramolecular electronic structure and intermolecular packing interactions governs properties such as magnetism, conductivity, and optical response. The interplay between electronic configuration, lattice distortions, and intermolecular interactions often gives rise to cooperative behavior in molecular frameworks. Subtle perturbations at the molecular scale can propagate through the lattice, leading to stepwise spin transitions, phase coexistence, or partial ordering of spin states. These phenomena are particularly relevant in materials exhibiting spin-crossover (SCO) behavior.

Spin-state ordering is commonly observed in SCO compounds, where the cooperative interconversion between high-spin (HS) and low-spin (LS) states produces correlated arrangements of spin centers within the lattice.[11–14] In classical SCO systems, non-symmetry-breaking transitions result in gradual changes in the HS/LS population with temperature. A change in molecular volume accompanies each transition, and when the lattice cannot accommodate the strain, symmetry breaking may occur.[14–16]

Theoretical approaches, including Landau theory[15] and elastic models,[15,17–20] have been used to rationalize complex SCO profiles, such as multi-step or incomplete transitions. These frameworks highlight the role of lattice elasticity and two distinct order parameters: the non-symmetry-breaking parameter q, which describes the electronic instability, and the symmetry-breaking parameter η, which captures structural rearrangements, both of which govern the SCO pathway. Stepwise, non-symmetry-breaking transitions have been reported in mononuclear Fe(II) complexes with two inequivalent sublattices in the asymmetric unit.[21] Each sublattice exhibits a distinct ligand-field environment and can be described by an independent order parameter (q_1, q_2).[15] Although chemically identical, these sublattices may undergo spin transitions at different temperatures, resulting in a global stepped response.[22–25]

Previous studies from our group have reported various SCO phenomena, including phase trapping, magnetic bistability,

[a]*Chemistry Department, Johannes Gutenberg University Mainz, Duesbergweg 10–14, 55128 Mainz, Germany. E-mail: rentschl@uni-mainz.de*
[b]*Institute of Physics of the Czech Academy of Sciences, Cukrovarnická 10, 162 00 Prague, Czech Republic*
[c]*Department of Physics, RPTU University Kaiserslautern-Landau, Erwin-Schrödinger-Str. 46, 67663 Kaiserslautern, Germany*

and spin-state ordering in 1,3,4-thiadiazole-based complexes, as well as mono- and dinuclear SCO complexes incorporating 1,3,4-oxadiazole ligands. In some cases, SCO is coupled with other functional properties, such as luminescence.[26–28]

Though the spin state of $3d^4$–$3d^7$ complexes is primarily determined by ligand-field strength, ligand-field effects alone do not fully account for the observed SCO behavior of Fe(II) complexes. Intermolecular interactions and crystal packing also play a decisive role.[29,30]

Herein, we report the synthesis of a tetradentate 1,3,4-thiadiazole-based ligand and its Fe(II) complexes with three different monodentate pseudohalide co-ligands (NCS^-, $NCSe^-$, and $NCBH_3^-$), providing a systematic platform to tune the ligand-field strength.[31–35] This series enables a direct correlation between molecular structure, crystal packing, and spin-state behavior. Notably, the NCS^- complex exhibits spin-state ordering at low temperature, highlighting the cooperative interplay between lattice packing and ligand-field effects. Comprehensive structural, magnetic, and spectroscopic analyses, complemented by DFT calculations, reveal how phase transitions govern the emergence of ordered spin states and provide fundamental insight into controlling SCO behavior in molecular materials.

Results and discussion

Synthesis

The ligand was synthesised according to the reaction scheme given in Fig. 1, with slight modifications to our previously reported ligand synthesis.[36] 1-(5-Phenyl-1,3,4-thiadiazole-2-yl)-*N*,*N*-bis(pyridin-2-ylmethyl)methanamine ($\mathbf{L^{Ph\text{-}TDA}}$) was synthesised in two steps. Starting from glycine, reductive amination with pyridinecarboxyaldehyde and sodium trisacetoxyborohydride in dichlormethane was performed to obtain bis(pyridine-2-yl)glycine (**I**) in low yields (30%).[37,38] The obtained product (**I**) was then further reacted with *N*,*N*′-carbonyldiimidazole (CDI) as coupling agent in dichlormethane coupled with benzohydrazide in a peptide-like coupling reaction *in situ* to obtain *N*′-(bis(pyridin-2-ylmethyl)glycyl)benzohydrazide.[39,40] Without any further purification or isolation, this was again further reacted *in situ* with Lawesson's reagent in dry tetrahydrofuran to obtain the desired 1-(5-phenyl-1,3,4-thiadiazol-2-yl)-*N*,*N*-bis(pyridin-2-ylmethyl)methanamine ($\mathbf{L^{Ph\text{-}TDA}}$) in high yields (85%).[41] The obtained ligand $\mathbf{L^{Ph\text{-}TDA}}$ was fully characterised by a range of techniques including ^{1}H-NMR-, ^{13}C-NMR-, 2D-NMR-, IR-spectroscopy and mass spectrometry.

The synthesis of the complexes was carried out under a nitrogen atmosphere and in dry acetonitrile by using the literature-reported precursor complexes $[Fe(py)_4(NCE)_2]$, with E = S, Se, and BH_3.[28] The desired complexes $[Fe(\mathbf{L^{Ph\text{-}TDA}})(NCE)_2]$ with E = S (**C1**), Se (**C2**) and BH_3 (**C3**) were obtained in moderate yields. In all three cases, the complexes obtained are air-stable and fully characterised using a range of techniques, including IR spectroscopy, which shows a principal peak at 2047 cm^{-1} and 2061 cm^{-1}, clearly confirming the formation of the complexes **C1** and **C2** by the characteristic C–N triple-bond stretching mode. Additionally, in the case of **C1**, the presence of a small shoulder close to 2047 cm^{-1} from the C–N triple bond suggests that the NCS co-ligands are bound to iron centers within two distinct coordination environments. For complex

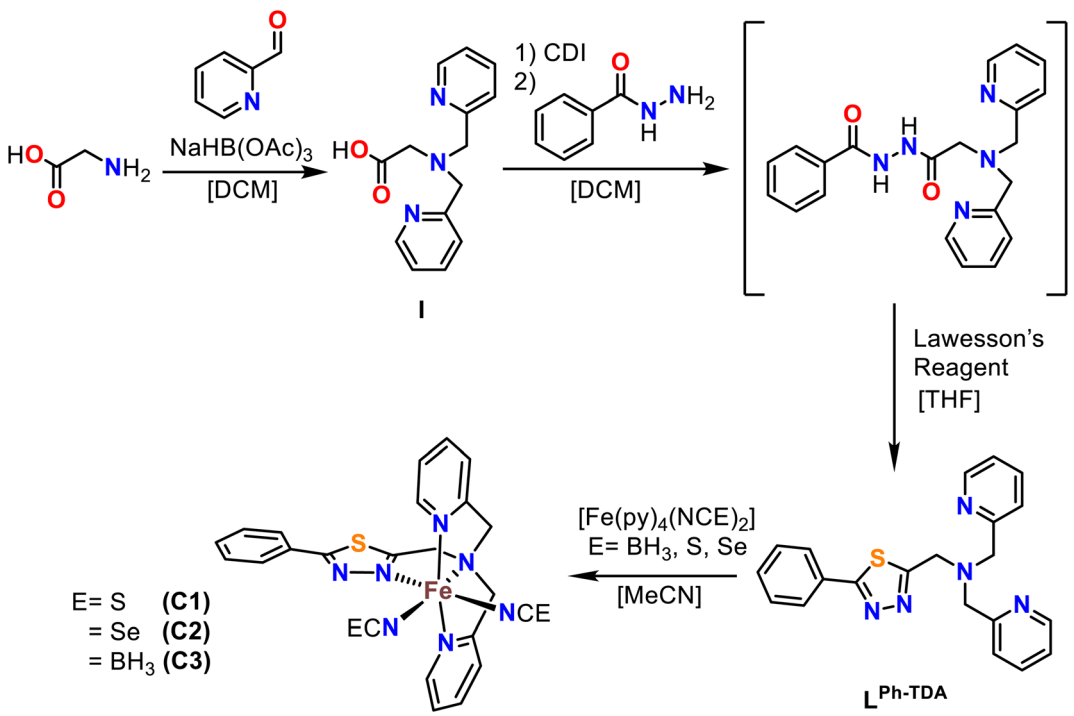

Fig. 1 Multi step synthetic scheme for synthesis of 1-(5-phenyl-1,3,4-thiadiazol-2-yl)-*N*,*N*-bis(pyridin-2-ylmethyl)methanamine ($\mathbf{L^{Ph\text{-}TDA}}$).

C3, the principal peak from the C–N triple bond is very close to the CO_2 peak around 2300 cm^{-1}; therefore, it is difficult to identify. However, it can still be observed in the CO_2-corrected spectrum at 2182 cm^{-1}. The reported values are consistent with those in the literature for Fe(II) complexes with NCE co-ligands.[31,35] The formation of the complex is also confirmed by shifts of the C–N vibrations of the 1,3,4-thiadiazole core, which are 1587 cm^{-1} and 1567 cm^{-1} compared to **C1** (1600 cm^{-1} and 1570 cm^{-1}), **C2** (1603 cm^{-1} and 1570 cm^{-1}) and **C3** (1604 cm^{-1} and 1571 cm^{-1}). These shifts indicate a change in electron density due to coordination, as reported for similar complexes with a 1,3,4-oxadiazole core (Fig. S8–S10).[32] The X-ray data for all three complexes were collected from single crystals carefully picked from the mother liquor, whereas magnetic data and IR spectroscopy were collected from the pure microcrystalline materials obtained from the same mother liquor by filtration. Wherever possible, variable-temperature X-ray data were collected to investigate changes in bond lengths and other structural parameters associated with spin crossover. The bulk samples analysed by elemental analysis indicate that, upon exposure to air over time, the lattice solvent is exchanged from acetonitrile to water in all cases. In the HRES mass spectrometry analysis of the complexes, the principal peak $[Fe(\mathbf{L}^{\mathbf{Ph\text{-}TDA}})(NCE)]^+$ was found in all three cases, with E = S (**C1**), Se (**C2**) and BH_3 (**C3**) confirmed by their corresponding isotopic patterns (Fig. S13–S18).

Temperature dependent magnetic properties

To evaluate the impact of variation in the NCE auxiliary ligand on the ligand field strength of the Fe(II) center, and consequently on the spin crossover (SCO) properties, the temperature dependence of the magnetic moments was examined for all three complexes (**C1–C3**). Temperature-dependent magnetic susceptibility ($\chi_M T$) was measured on pure microcrystalline samples over 10–300 K under heating and cooling.

A $\chi_M T$ value of 3.09 at room temperature and 2.87 cm^3 K mol^{-1} at 50 K confirms that the **C2** complex remains in the high-spin state across the entire temperature range (see Fig. 2, blue curve). These values are in excellent agreement with literature data for mononuclear high-spin (HS) Fe(II) complexes, which typically exhibit magnetic moments in the range of 3–4 cm^3 K mol^{-1}.[29,42] The slight decrease in the $\chi_M T$ value below 50 K can be attributed to a combination of weak intermolecular dipolar interactions and the zero-field splitting effects of the Fe(II) center.

In contrast, complex **C3** undergoes a complete one-step spin transition centered around 170 K ($T_{1/2}^{down} = T_{1/2}^{up} = 170$ K). This is clearly reflected in the change in $\chi_M T$ from 0.08 cm^3 K mol^{-1} at low temperatures to 2.96 cm^3 K mol^{-1} at higher temperatures. When this SCO behavior is compared to that of the related 1,3,4-oxadiazole analog, $[Fe(\mathbf{L}^{\mathbf{Ph\text{-}ODA}})(NCBH_3)_2]\cdot 0.8H_2O\cdot 0.5CH_3OH$, it is worth noting that the spin transition in **C3** occurs more gradually over a 50 K range, likely due to lattice and solvent effects, as well as differences in crystal packing, which will be discussed in detail later.[33] However, the slight shift in $T_{1/2}$ from 166 K, for the oxadiazole-based complex, to 170 K, for the thiadiazole-based analog, indicates only a small increase in ligand field strength upon replacing the 1,3,4-oxadiazole moiety with a 1,3,4-thiadiazole unit.[33] A more pronounced effect seems to arise from the change in the ligand field strength imposed by the $NCSe^-$ co-ligands. While **C2**, which contains $NCSe^-$ co-ligands, remains in the HS state throughout the 10–300 K range, **C3**, which contains stronger $NCBH_3^-$ co-ligands, exhibits a well-defined spin transition at 170 K.

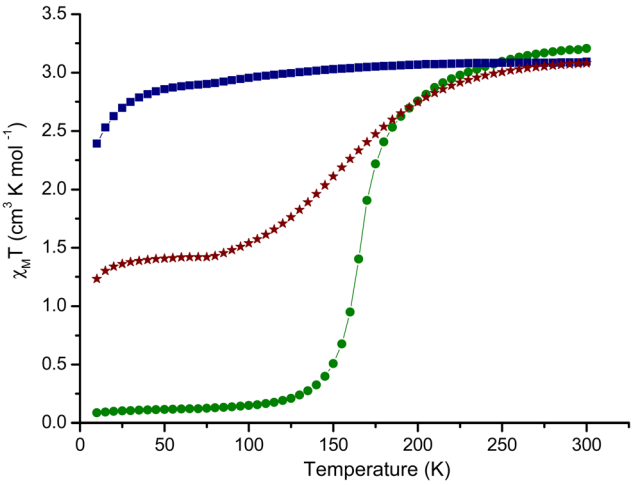

Fig. 2 Temperature dependence of the molar susceptibility based on one $[Fe(\mathbf{LPh}^{\mathbf{TDA}})(NCE)_2]$ unit with E = S (**C1**; red, ✱), Se (**C2**; blue, ■) and BH_3 (**C3**; green, ●) depicted in $\chi_M T$ *vs.* *T*. The magnetic susceptibilities were determined between 300–10 K and 10–300 K and the additional data are shown in the SI (Fig. S52–S55). The circle, square and stars represent the data, while the lines are just guides for the eye.

Based on this trend, it was expected that **C1**, with the weakest co-ligand (NCS^-), would remain in the HS state throughout the temperature range, as would **C2**. At room temperature, the observed $\chi_M T$ value of 3.08 cm^3 K mol^{-1} for one $[Fe(\mathbf{L}^{\mathbf{Ph\text{-}TDA}})(NCS)_2]$ unit closely matches the values reported in the literature for HS Fe(II) species, and is in good agreement with those of **C2** and **C3**. However, upon cooling, the $\chi_M T$ value gradually decreases to 1.41 cm^3 K mol^{-1} and reaches a plateau between 30 and 85 K, with a $T_{1/2}$ value of 153 K. The spin switch occurs at higher temperatures than for **C2** with NCSe and at lower temperatures than for **C3** with $NCBH_3$. This behavior deviates from the expected trend based solely on ligand field strength. The observation of an incomplete spin crossover in **C1** can be attributed to several structural and lattice-related factors commonly encountered in Fe(II) SCO systems. Partial conversion from the HS to the LS state is often the result of crystal packing constraints, which leave a fraction of the molecules in the HS configuration. Additionally, kinetic trapping of the HS species during cooling cannot be excluded *a priori*. Assuming negligible contribution to the magnetic moment from the low-spin (LS) Fe(II) state ($^1A_{1g}$, $S = 0$), the plateau value of 1.41 cm^3 K mol^{-1} at 50 K indicates that 46% of the Fe(II) centers are trapped in the HS state.

To further substantiate the partial SCO behavior observed for **C1**, variable-temperature Mössbauer spectroscopy (*vide infra*) and a thorough analysis of the structural data were performed.

Structural characterization and spin crossover behavior of complexes C1–C3

Single crystals of the three complexes [Fe($\mathbf{L}^{\mathbf{Ph\text{-}TDA}}$)(NCE)$_2$]·solvent (E = SCN (**C1**), SeCN (**C2**), BH_3CN (**C3**)) were investigated by variable-temperature single-crystal X-ray diffraction (SC-XRD) at 120 K and 240 K (**C1**) or 230 K (**C3**). Complex **C1** [Fe($\mathbf{L}^{\mathbf{Ph\text{-}TDA}}$)(NCS)$_2$]·$H_2O$(0.5MeCN) crystallises in the triclinic space group $P\bar{1}$, containing two independent [Fe($\mathbf{L}^{\mathbf{Ph\text{-}TDA}}$)(NCS)$_2$] units and one solvent molecule in the asymmetric unit. Both complexes **C2** and **C3** ([Fe($\mathbf{L}^{\mathbf{Ph\text{-}TDA}}$)(NCE)$_2$]·MeCN, E = Se, BH_3) crystallise in the monoclinic *C*2/*c* space group. Each has one crystallographically independent complex and 2.5 acetonitrile molecules in the asymmetric unit. Key crystallographic parameters are provided in Tables S3–S7.

Each Fe(II) center in all three complexes is octahedrally coordinated by one tetradentate $\mathbf{L}^{\mathbf{Ph\text{-}TDA}}$ ligand and two *cis*-positioned pseudohalide co-ligands (NCS^-, $NCSe^-$, or $NCBH_3^-$). Depending on the co-ligand and temperature, the resulting FeN_6 cores display varying degrees of angular and bond-length distortion. At 120 K, **C1** exhibits two distinct iron sites: Fe1 and Fe2 (Fig. 3). At 240 K, both are in the HS state with an average Fe–N distance of 2.18 Å (Fe1) and 2.16 Å (Fe2). Upon cooling to 120 K, Fe1 remains in the HS state with an average Fe–N distance of 2.17 Å, while Fe2 contracts to 1.98 Å. This indicates that only Fe2 undergoes an HS → LS transition.[33,34] This is also reflected in the trigonal twist angle, which decreases from 92.8° at 240 K to 43.9° at 120 K for Fe2, but changes only slightly for Fe1 (109.3° → 108.1°).[43]

For **C2**, the Fe atom is disordered over two positions (85 : 15 ratio) with average Fe–N bond distances of 2.17 ± 0.08 Å and 2.06 ± 0.11 Å, and corresponding distortion parameters of 101.7° and 49.6°, respectively.[33,43] These values are consistent with the high-spin configuration. Finally, in **C3**, no Fe-site disorder is observed. The average Fe–N distance at 120 K is 1.97 ± 0.02 Å, characteristic of the LS state, whereas at 230 K it increases to 2.15 ± 0.05 Å, indicative of a HS state.[33,43] The distortion parameter rises from 49.6° to 86.9°, confirming a thermally induced spin crossover (SCO) (Fig. 4).

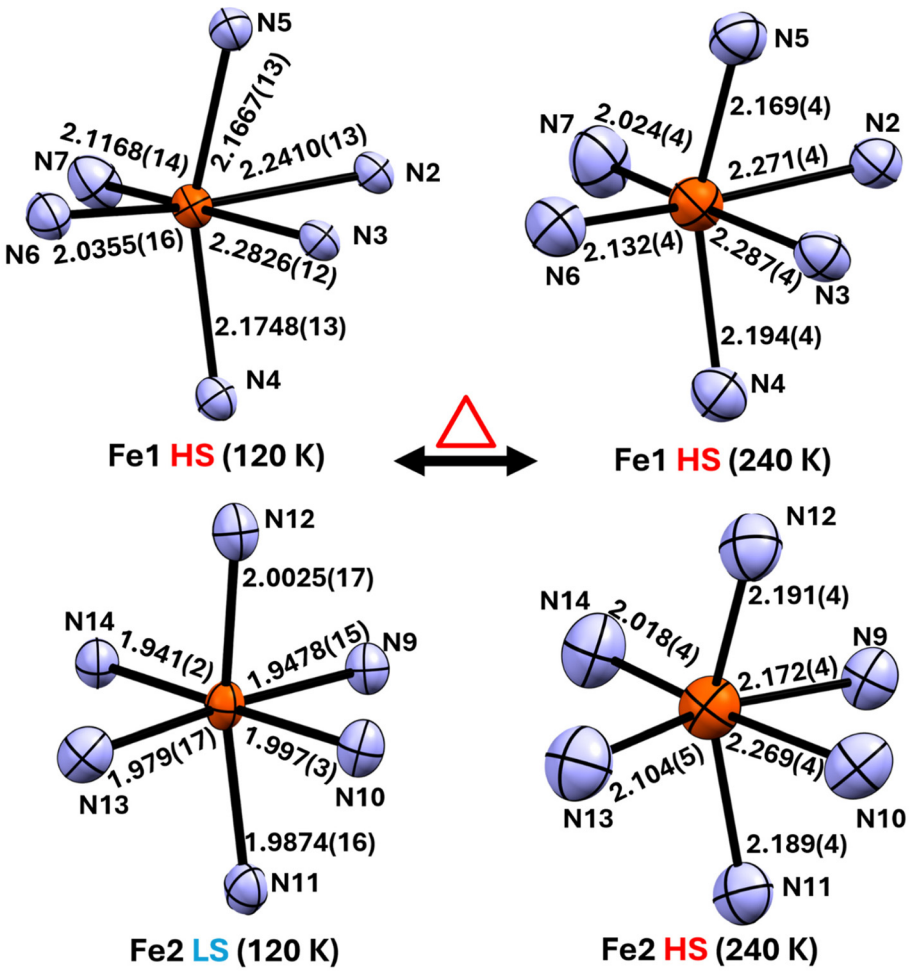

Fig. 3 Iron(II)–nitrogen bond lengths for the two crystallographically independent, Fe1 and Fe2, iron(II) centers, in **C1** at 120 K and 240 K.

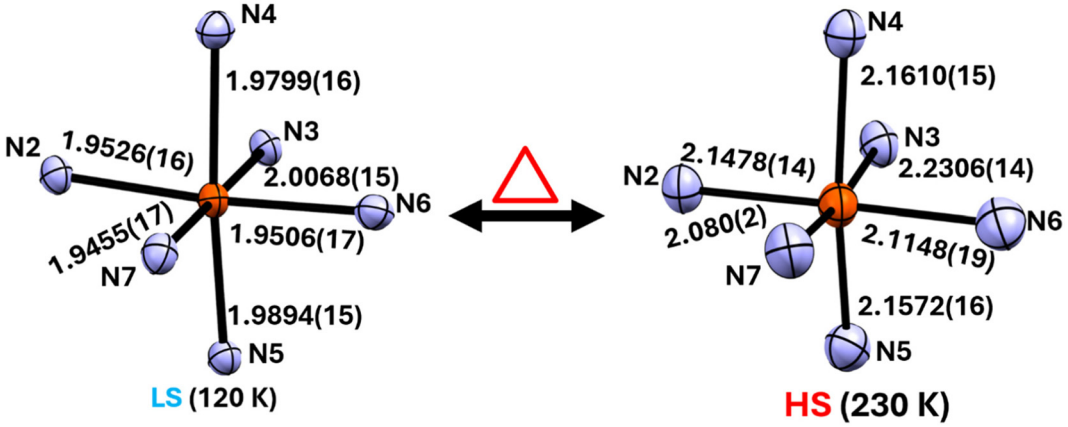

Fig. 4 Metal donor bond distances at 120 and 230 K for [Fe(**LPh**$^{-}$**TDA**)$(NCBH_3)_2]\cdot H_2O$ (**C3**).

Comparison of **C2** and **C3** cell parameters according to the relation

$$\Pi = \frac{(a+b+c)}{(a'+b'+c')} - 1 = 0.008$$

(B. Ribár *et al.*[44]) indicates that both are isostructural and isomorphous, despite differing co-ligands.[31,32,45] Their nearly identical cell volumes (**C2**: 6508 Å^3; **C3**: 6439 Å^3 at 120 K) support this conclusion. At 230 K, the cell volume of **C3** increases by about 4%, consistent with a spin-state change from LS to HS. In contrast, **C2** remains essentially unchanged, confirming a locked HS configuration.

Packing motifs play an important role in modulating the SCO behavior of complexes.[46] Thus, the intermolecular interactions of the complexes **C1–C3** are discussed in more detail here. In **C2** and **C3**, adjacent [Fe(**L**$^{\mathbf{Ph\text{-}TDA}}$)$(NCE)_2$] molecules form dimers *via* strong π–π interactions between the 5-phenyl-1,3,4-thiadiazole rings, with plane-to-atom distances of 3.558 Å (**C2** at 120 K), 3.377 Å (**C3** at 120 K), and 3.523 Å (**C3** at 230 K). Beyond these dimers, only weak π–π interactions are present between the tilted pyridyl rings (Fig. S39, S40, S45, S46, S50 and S51). Solvent molecules occupy channels along the *c*-axis, where the sulfur atoms of the thiadiazole rings and the Se or BH_3 atoms/groups of the co-ligands point toward the interior (Fig. S38, S44 and S49). The complexes therefore behave as isolated π–π-linked dimers, with limited long-range cooperativity.

In **C1**, the packing arrangement is distinctly different. Two types of [Fe(**L**$^{\mathbf{Ph\text{-}TDA}}$)$(NCS)_2$] units (Fe1 and Fe2) are present, forming homologous pairs (Fe1–Fe1, Fe2–Fe2) separated by confined solvent molecules rather than channels. The Fe1–Fe1 dimers exhibit strong π–π stacking between the thiadiazole and phenyl groups, with plane-to-atom distances of 3.309 Å at 120 K and 3.376 Å at 240 K. These distances are even shorter than those in **C2** and **C3**, indicating particularly strong π–π coupling. No additional hydrogen bonds or π–π interactions are observed.[46] The Fe2–Fe2 pairs, in contrast, are more weakly connected: the 5-phenyl-1,3,4-thiadiazole rings are co-planar but laterally shifted, reducing the orbital overlap. Weak π–π interactions between pyridyl moieties connect these pairs into zig-zag chains, creating a more flexible lattice environment. This structural softness enables partial SCO in **C1**, localised to the Fe2 sublattice.

Changes in the Fe–N bond length and the resulting change in the unit cell volume clearly demonstrate the distinct SCO behavior throughout the series. For complex **C1**, only the Fe2 sites undergo conversion to the low-spin (LS) state upon cooling, while the Fe1 sites remain in the high-spin (HS) configuration. The coexistence of HS and LS centers within the same lattice gives rise to spin-state ordering. The unit-cell volume changes only slightly, from 2515 Å^3 at low temperature to 2620 Å^3 at high temperature, consistent with approximately 50% of the Fe(II) centers switching. In the case of **C2**, all structural parameters confirm a stable HS configuration throughout the entire temperature range investigated. By contrast, complex **C3** exhibits a complete and gradual SCO, as evidenced by both SC-XRD and magnetic measurements. Upon warming, the average Fe–N bond lengths increase from 1.97 Å to 2.15 Å, accompanied by a rise in the distortion parameter from 49.6° to 86.9°, and an expansion of the unit-cell volume by about 4%.[46]

Overall, the combination of structural rigidity, π–π coupling, and ligand-field strength dictates the degree and cooperativity of spin crossover in these Fe(II) complexes. The three derivatives [Fe(**L**$^{\mathbf{Ph\text{-}TDA}}$)$(NCE)_2$] (E = S, Se, BH_3) display markedly different behaviors: **C1** exhibits sublattice spin-state ordering at low temperatures, **C2** remains locked in the HS state, and **C3** undergoes a complete, one-step SCO with $T_{1/2}$ = 153 K.

Variable-temperature Mössbauer spectroscopy

As illustrated in Fig. 5 and Table 1, the Mössbauer spectrum at 77 K was analyzed using two components, each with a 50% relative contribution, that can be assigned to two different iron centers in **C1**. Component 1 shows an isomer shift δ =

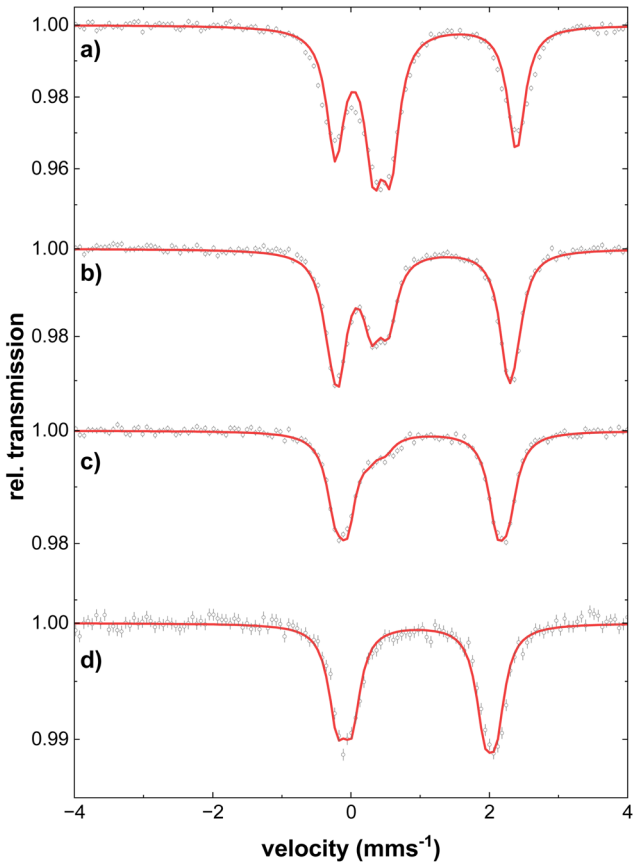

Fig. 5 Mössbauer spectra of compound **C1** at (a) 90 K, (b) 150 K, (c) 210 K and (d) 270 K. The open circles show the experimental data obtained at the respective temperatures, the red solid lines represent simulations based on Lorentzian line shapes. The simulation parameters are listed in Table 1.

1.08 mm s^{-1} and a quadrupole splitting ΔE_Q = 2.62 mm s^{-1}. These parameters are characteristic of an HS iron(II) in an octahedral ligand field and are assigned to the HS state of Fe1.[47] Component 2, on the other hand, exhibits δ = 0.45 mm s^{-1} and ΔE_Q = 0.25 mm s^{-1}. Such low values of the isomer shift and quadrupole splitting can be attributed to an LS iron(II) ion in an octahedral field and are assigned to the LS state of Fe2.[47]

With increasing temperature, component 3 emerges showing δ = 1.04 mm s^{-1} and ΔE_Q = 2.71 mm s^{-1} and a relative contribution of 19% at the cost of component 2 at 150 K (Fig. 5b). These parameters are typical of HS iron(II). Therefore, component 3 is assigned to the HS state of Fe2. This shows that a thermal spin transition from the LS to the HS state occurs in Fe2. In contrast, increasing the temperature results in nearly constant values of the isomer shift and quadrupole splitting for Fe1 (component 1). Only δ is slightly reduced due to the second order Doppler shift. This means that Fe1 is in the HS state at all experimentally accessible temperatures, which is consistent with the magnetic susceptibility measurements and supports the structural analysis's conclusions. Further increase of the temperature to 270 K leads to the complete spin transition to the HS state of Fe2 (Fig. 5d) in perfect agreement with the magnetic measurements and the crystal structure.

DFT modelling

For the [Fe($\mathbf{L}^{\mathbf{Ph\text{-}TDA}}$)(NCE)$_2$] complexes with E = S (**C1**), Se (**C2**) and BH_3 (**C3**), clearly the packing effects play just as significant a role as the ligand field strength. In the isomorphous structures of **C2** and **C3** the ligand field strength is the crucial factor to observe spin transition or not. With a weaker ligand field induced by the $NCSe^-$ ligands no spin transition can be observed (**C2**), while the stronger ligand field of $NCBH_3^-$ leads to a spin crossover at 170 K. For **C1** the packing is obviously the most important factor. Although the coordination environments of [Fe1($\mathbf{L}^{\mathbf{Ph\text{-}TDA}}$)(NCS)$_2$] and [Fe2($\mathbf{L}^{\mathbf{Ph\text{-}TDA}}$)(NCS)$_2$] are nearly identical, their behaviour is completely different when cooled. Thus, we examined the elastic effects of packing *via* DFT calculations.

First, we calculated the ground state energies of the HS (E_{HS}) and the LS (E_{LS}) states for the isolated molecules **C1–C3**. This yields the electronic spin transition energies $E_{el}^{iso} = E_{HS} - E_{LS}$. Next, for compound **C1** we estimated the effect of the lattice which has a spin occupation of HS : LS = 1 : 1 at low temperatures on the spin transition energies of the sites Fe1 and Fe2. For this purpose, we used the method recently proposed by us.[48]

In this approach, spin transition energies are calculated in the E_{el}^{cryst} model by optimizing the geometry of the LS and HS states of the molecules in the environment of their neighbours, using coordinates taken from the crystal structure. The geometry of the neighbours remains fixed. For **C1** a model containing 22 complex molecules and 11 MeCN molecules,

Table 1 Mössbauer parameters of Fe1 and Fe2 of the complex **C1** as obtained from the analysis of the experimental data displayed in Fig. 5. The line width Γ is 0.30(2) mm s^{-1} for all components

	Fe1			Fe2					
	Component 1			Component 2			Component 3		
T [K]	δ [mm s^{-1}]	ΔE_Q [mm s^{-1}]	Area [%]	δ [mm s^{-1}]	ΔE_Q [mm s^{-1}]	Area [%]	δ [mm s^{-1}]	ΔE_Q [mm s^{-1}]	Area [%]
90	1.08(2)	2.62(3)	50	0.45(3)	0.25(4)	50			
150	1.05(2)	2.46(3)	50	0.42(3)	0.24(4)	31(3)	1.04(2)	2.71(3)	19(3)
210	1.03(2)	2.16(3)	50	0.38(3)	0.23(4)	9(3)	1.02(2)	2.51(3)	41(3)
270	0.97(2)	1.92(3)	50				0.95(2)	2.30(3)	50

which are present in the crystal lattice, was used. As in the previous paper the high-spin molecules that were not optimised were replaced by the diamagnetic Zn(II) analogues in order to minimise the computational effort.[48] The observed disorder arising from the deviation of the 5-phenyl-1,3,4-thiadiazole moieties at the Fe1 pairs in the single-crystal structure of **C1** was neglected in the model, since it has no influence. As the inversion centre lies between the moieties, both isomers are present in equal amounts and thus have the same intermolecular interactions. Furthermore, the disorder associated with Fe2 and the NCS coligand was also disregarded, as it corresponds to partially unswitched high-spin Fe(II). At temperatures below 85 K, the system exhibits a 50 : 50 distribution of high-spin (HS) and low-spin (LS) Fe(II). Since the crystal structure was measured at 120 K, the disorder was not explicitly modelled. The model used is depicted schematically in Fig. 6. The optimised structures are given as pdb and xyz files in SI.

Two molecules at the centre of the model assembly were optimised for four possible spin states: both in the LS state (LS-Fe1–LS-Fe2) (3); both in the HS state (HS-Fe1–HS-Fe2) (4); Fe1 in the HS state and Fe2 in the LS state (HS-Fe1–LS-Fe2, corresponding to the crystal structure at low temperatures) (1); and Fe1 in the LS state and Fe2 in the HS state (LS-Fe1–HS-Fe2) (contrary to what is observed in the crystal structure) (2). Details of how the particular spin distributions were achieved can be found in the Computational methods section in the SI. The geometry of the other thirteen complex molecules and the solvated acetonitrile molecules was frozen. The optimised systems are provided as PDB files in the SI. The combined results are given in Table 2.

The absolute values of the obtained electronic spin transition energies E_{el} are highly dependent on the applied exchange–correlation functional.[48,49] Therefore, it is important to compare the obtained values within a series of related mole-

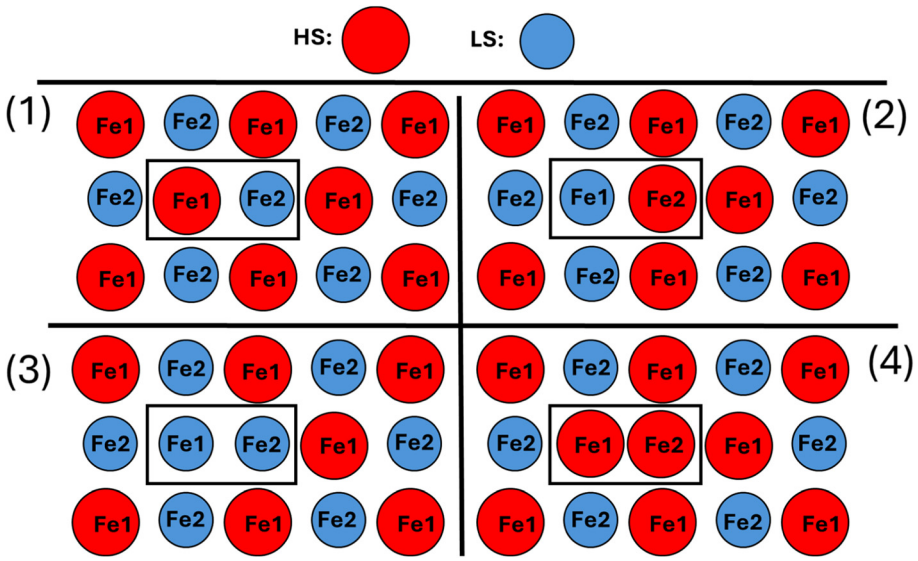

Fig. 6 Graphic representation of the model of the low-temperature crystals structure of **C1** used for the DFT calculations for the four cases considered: (1) HS-Fe1–LS-Fe2 (as observed in the crystal structure), (2) LS-Fe1–HS-Fe2 (inverse to the situation observed in the crystal structure), (3) LS–LS and (4) HS–HS. The complexes are simplified by circles (red = high spin state iron(II)) and blue circle (low spin state state). The molecules in the black box were optimised. The molecules out of the box, as well as MeCN, were kept frozen during optimization. To reduce the computational time, the frozen Fe2 molecules were modelled as the Zn(II) analogues.

Table 2 First column: DFT (CAM-B3LYP/CEP-31G/D3) calculated values of E_{el}^{iso} in (kJ mol^{-1}) for **C1**, **C2** and **C3**. Second column: electronic energies of the three different spin isomers of the **C1** crystal model taken relative to the HS-Fe1–HS-Fe2 spin isomer model. Third column: spin transition energies to the 2HS isomer. Fourth column: calculated values of $H_{elastic}$

Isolated molecule/E_{el}^{iso}		Models of crystal of **C1**/ relative electronic energies		E_{el}^{cryst}		$H_{elastic}$
C1	−34	LS-Fe1–LS-Fe2	37[a]	[2LS → 2HS][a]	−37	−31[a]
C2	−28	HS-Fe1–LS-Fe2	19	[Fe1^{HS}Fe2^{LS} → 2HS]	−19	−15
C3	−21	LS-Fe1–HS-Fe2	29	[Fe1^{LS}Fe2^{HS} → 2HS]	−29	−5
		HS-Fe1–HS-Fe2	0			
[Fe(L^{npdtz})$_2$(NCS)$_2$][b]	−18			[LS → HS] LS matrix	−9	−9
				[LS → HS] HS matrix	−20	2

[a] For two switching centres. [b] Ref. 48.

cules/molecular assemblies. In this respect, the calculated values for the isolated complex molecules **C1–C3** suggest that **C3** (E_{el}^{iso} = −21 kJ mol^{-1}) is the molecule with the lowest stabilization of the HS state. This is the only one of the three systems displaying the full HS-to-LS transition in the 300–10 K range. The calculated energies of the isolated molecules are in perfect agreement with the increase in ligand field strength from NCS^- < $NCSe^-$ < $NCBH_3^-$. Stronger ligand field strength stabilizes the LS *versus* the HS *i.e.* destabilizes the HS *versus* the LS in the order **C3** > **C2** > **C1**. Complex **C1** with the lowest value of E_{el}^{iso} = −34 kJ mol^{-1} shows partial switching of the iron(II). This leads to the conclusion that packing effects present in the crystal lattice of **C1** allow the LS state for 50% of the molecules at low temperatures.

Modelling four **C1** structures using a 22-molecule assembly reveals the relative energies of four different spin-state distributions in Fe1 and Fe2, while keeping the matrix identical to that of the crystal structure of the low-temperature phase of **C1**.

(i) The HS-Fe1–HS-Fe2 spin isomer has the lowest energy, while the LS-Fe1–LS-Fe2 spin isomer has the highest energy.

(ii) The HS-Fe1–LS-Fe2 spin isomer, which corresponds to that observed at low temperatures, is 19 kJ mol^{-1} higher in energy than the HS-Fe1–HS-Fe2 isomer and 10 kJ mol^{-1} lower than the LS-Fe1–HS-Fe2 isomer, *i.e.*, the isomer with the inverted spin distribution of the Fe1 and Fe2 centers. This result indicates the influence of the crystal lattice of the low-temperature phase, in which the LS-Fe1–HS-Fe2 spin isomer is a double-center defect. To quantify the effect of the lattice on the spin transition energies compared to that calculated for the isolated molecules we now introduce the parameter $H_{elastic}$, which we define as the difference between the spin transition energy calculated for the isolated molecule E_{el}^{iso} and the spin transition energy obtained for the model crystal E_{el}^{cryst}. It is well known that E_{el}^{iso} reflects the effects of the ligand field differences between spin isomers that may be tuned by the ligand strain effects.[51] In addition to the ligand field differences, E_{el}^{cryst} also contains contributions from intermolecular interactions in the crystal and hence reflects the elastic interaction between the lattice and the center of a given spin.

In our model system there are three possible spin transitions: (i) LS Fe1 and LS Fe2 undergo spin transition: [2LS → 2HS], (ii) Fe1 remains HS and only Fe2 undergoes spin transition: [$Fe1^{HS}Fe2^{LS}$ → 2HS], and (iii) Fe2 remains HS and only Fe1 undergoes spin transition: [$Fe1^{LS}Fe2^{HS}$ → 2HS].

For (i) [2LS → 2HS] we have calculated $H_{elastic}$ = −31 kJ mol^{-1} (2 × −34 + 37) which amounts to −15.5 kJ mol^{-1} per Fe(II) centre. That suggests an average stabilization of the LS-pair with one LS-defect compared to the isolated molecules. For (ii) [$Fe1^{HS}Fe2^{LS}$ → 2HS] we obtain $H_{elastic}$ = −15 kJ mol^{-1}, pointing to a similar stabilization of the LS-state in the lattice, compared to the isolated molecule. For (iii) [$Fe1^{LS}Fe2^{HS}$ → 2HS] we get $H_{elastic}$ = −5 kJ mol^{-1}, indicating a low effect of the lattice on the LS → HS spin transition in the matrix corresponding to the low-temperature structure. Hence, the results imply generally the stabilisation of the low-spin state by the 1 : 1 HS–LS lattice compared to the isolated molecule, the effect being the lowest when the observed occupation of sites Fe(1) and Fe(2) by the high-spin and low-spins molecules, respectively is reversed. The calculated spin transition values for the related [$Fe(L^{npdtz})_2(NCS)_2$] complex we give the $H_{elastic}$ values of −9 and 2 kJ mol^{-1} for the LS- and HS-lattice model, respectively pointing to a stabilisation of the low-spin state by the low-spin matrix.[48]

A further insight into the effects of 1 : 1 LS : HS matrix on the energy and geometry of the "defects" may be obtained by comparing the structures of the optimised low-spin and high-spin molecules for all four patterns of occupation of the Fe(1) and Fe(2) sites. For this purpose, we performed the point-energy calculations for the optimised molecules in (LS-Fe1–LS-Fe2), (HS-Fe1–HS-Fe2), (HS-Fe1–LS-Fe2) and (LS-Fe1–HS-Fe2) pairs. The results are given in Table 3.

It seems that the LS centre has two possible structures, corresponding to the "regular" one, observed in X-ray for Fe(2) and the "defect" one differing at 6 kJ mol^{-1} in energy.

In Table 4 we compare the calculated bond lengths for three possible distributions of the low-spin state between Fe(1) and Fe(2) sites, *i.e.* two LS/HS systems and the LS/LS one. It is evident that the low-spin Fe(2) in HS-Fe1–LS-Fe2 and LS-Fe1–LS-Fe2 models are the same, with the larges difference to be 0.002 Å for one of the Fe–N_{py} bond. Similar consistency occurs for the two structures bearing a low-spin defect in Fe(1) site. The main structural difference between the "regular" and "defect" geometry is the average 0.0365 Å elongation of the Fe–$N_{thiazole}$ bond for the latter. No other bond reveals a particular distance difference for both structures. Hence, solely the above-mentioned elongation in the "defect" structures brings about the 6 kJ mol^{-1} increase in it energy.

The obtained results for the high-spin bond lengths are collected in Table 5. Again, it seems that both "regular" HS structures are nearly identical, with largest differences given for one

Table 3 Calculated relative energies (point energies of the isolated molecules) of the low-spin and high-spin molecules for the Fe(1)–Fe(2) pair optimised with the 22-molecule models of the different spin distributions. The lowest value of four obtained was taken to be zero. The energies of the "defects" in the LS : HS matrix are given in italics

			LS-Fe1–LS-Fe2		HS-Fe1–HS-Fe2	
	HS-Fe1–LS-Fe2	LS-Fe1–HS-Fe2	Fe(1)	Fe(2)	Fe(1)	Fe(2)
E_{LS}/kJ mol^{-1}	0	*6*	*6*	0		
E_{HS}/kJ mol^{-1}	1	*5*			0	*4*

Table 4 Calculated low-spin Fe–N distances (in Å) for the "regular" (low-spin Fe(2)) and "defect" ones (low-spin Fe(1)) structures for the optimised models of three spin distributions of the low-spin state. The values for the "defect" are given in italics

			LS-Fe1–LS-Fe2	
	HS-Fe1–LS-Fe2	LS-Fe1–HS-Fe2	Fe(1)	Fe(2)
$Fe–N_{thiazole}$	1.968	*2.004*	*2.006*	1.969
$Fe–N_{Nsp3}$	2.051	*2.048*	*2.047*	2.052
$Fe–N_{py}$	1.996, 1.996	*1.990, 2.006*	*1.990, 2.006*	1.995, 1.996
$Fe–N_{NCS}$	1.958, 1.967	*1.952, 1.971*	*1.952, 1.973*	1.959, 1.969

Table 5 Calculated high-spin Fe–N distances (in Å) for the "regular" high-spin structure of the regular (high-spin Fe(1)) and "defect" ones (high-spin Fe(2)) for the optimised models of three spin distributions of the high-spin state. The values for the "defect" are given in italics

			HS-Fe1–HS-Fe2	
	HS-Fe1–LS-Fe2	LS-Fe1–HS-Fe2	Fe(1)	Fe(2)
$Fe–N_{thiazole}$	2.192	*2.146*	*2.144*	2.191
$Fe–N_{Nsp3}$	2.305	*2.311*	*2.312*	2.306
$Fe–N_{py}$	2.142, 2.142	*2.138, 2.161*	*2.139, 2.162*	2.143
$Fe–N_{NCS}$	2.141, 2.040	*2.113, 2.067*	*2.109, 2.063*	2.136, 2.039

of the $Fe–N_{NCS}$ bonds (0.005 Å), while the "defect" ones match equally well with the largest differences found in one of the $Fe–N_{NCS}$ bonds (0.004 Å). Similarly, the only pronounced change on going from the "regular" and "defect" structures concerns the $Fe–N_{thiazole}$, which is on average 0.0465 Å shorter for the "defect" structures. This pattern, together with a bit lower energetic effect of distortion effect for the high-spin isomers resembles the general pattern of elongation of the low-spin bonds and shortening of the high-spin upon distortion by the lattice.[48,49]

Conclusions

In summary, we have introduced a new 1,3,4-thiadiazole-based tetradentate ligand, $\mathbf{L^{Ph\text{-}TDA}}$, and demonstrated its ability to stabilize distinct spin states in a family of iron(II) complexes, $[Fe(\mathbf{L^{Ph\text{-}TDA}})(NCE)_2]$ (E = S, Se, BH_3). The series of complexes, **C1–C3**, reflects the dependence of spin-crossover (SCO) behavior on the ligand-field strength of the coordinated pseudohalides, following the order $NCS^- < NCSe^- < NCBH_3^-$. In **C1**, the weaker NCS^- co-ligand generates a small ligand-field splitting and a distorted coordination environment, giving rise to sublattice spin-state ordering at low temperature: π–π-stacked Fe1 dimers remain locked in the high-spin (HS) state, while more flexible Fe2 sites undergo partial SCO. In **C2**, substitution by the slightly stronger $NCSe^-$ co-ligand enhances the ligand field, but due to packing effects, **C2** remains locked in the HS state throughout the measured temperature range. By contrast, **C3**, containing the strongest-field $NCBH_3^-$ co-ligand, stabilizes the low-spin (LS) state at low temperature and undergoes a complete SCO centered around $T_{1/2}$ = 153 K.

The observation of ordered LS–HS sublattices in **C1** underscores the delicate balance between electronic and cooperative effects that dictates bistability. Complementary DFT calculations provide quantitative insight into the energetics of the spin states, clarifying the role of ligand-field strength, coordination geometry, and the choice of co-ligand in collectively determining SCO behavior. Together, these results position the $(\mathbf{L^{Ph\text{-}TDA}})$–Fe(II)–NCE framework as a versatile platform for engineering spin-state ordering and controllable SCO phenomena, advancing design principles for multifunctional molecular switches and enabling the rational exploitation of ordered spin states and photoinduced phase transitions in responsive magnetic materials.

Experimental

All chemicals were purchased from Deutero, Fisher Chemicals, TCI, Sigma-Aldrich BLD Pharma and Carbolution used without further purification. Solvents were dried according to the literature known procedures and used freshly distilled. NMR spectra were recorded at room temperature with a Bruker Avance DSX 400 and analyzed with the program MestReNova.[50] Magnetic susceptibility measurements were performed on a Quantum Design SQUID magnetometer MPMSXL in a temperature range between 5 and 300 K with an applied field of 1 kOe. The ATR-IR spectra was recorded at room temperature on a Bruker ALPHAII ATR-IR, analysed with the software OPUS and plotted in Origin 7.5 V5. HRes ESI mass spectra were recorded on Agilent 6200 series TOF/6500 series G-TOF (11.0.203.0) at Johannes Gutenberg-University Mainz in acetonitrile. Elemental analysis (Elementar vario EL Cube: C, H, and N) were measured at the microanalytical laboratories of the Johannes Gutenberg University Mainz. Solid State UV-Vis measurement were done with following setup: synchronous scans of the solid sample and the reference (PTFE plate) were

measured with a FLS1000 spectrometer from Edinburgh Instruments equipped with a cooled photomultiplier detector PMT-980 and $BaSO_4$ was used as matrix. A xenon arc lamp Xe2 (450 W) was used for excitation. The measurements were carried out using a liquid nitrogen cooled MicrostatN from Oxford Instruments combined with the Cryosphere from Edinburgh Instruments. X-ray diffraction data were collected with STOE STADIVARI at the Johannes Gutenberg University Mainz. The structures were solved with ShelXT and refined with ShelXL implemented in the program Olex2.[51–53] The X-ray cif file data are deposited on the Cambridge CCDC database with identification numbers 2480291–2480295.

Mössbauer experiments were performed in transmission geometry in time-scale mode in conjunction with a 512-channel analyzer (WissEl GmbH, Starnberg, Germany). Variable temperature measurements were performed using a contiuous flow cryostat (Optistat^{DN}, Oxford Instruments, Abingdon, UK). The radioactive source consisted of ^{57}Co diffused in Rh with an activity of 1.67 GBq. The calibration of the spectrometer was carried out against α-iron at room temperature. The analysis of the spectral data was accomplished using least-squares fits and Lorentzian line shapes employing the public domain program Vinda running on Excel 2003® platform.[54]

DFT calculations were performed with Gaussian 16 [55] using the CAM-B3LYP[56] functional and the cep-31g basis[57–59] set with Grimme D3 dispersion correction.[60] Further details of calculations are given in SI.

Ligand synthesis

Bis(pyridine-2-yl)glycine (I). Glycine (3.00 g, 79.93 mmol, 1.0 eq.) was suspended in 80 mL DCM under nitrogen atmosphere. Under cooling with ice sodium trisacetoxyborohydride (21.18 g, 99.91 mmol, 2.5 eq.) was added and stirred. After 10 minutes a solution of 2-pyridinecarbaldehyde (7.60 mL, 79.93 mmol, 2.0 eq.) in 20 mL dichloromethane was added. The cooling was replaced, and the yellowish suspension was allowed to warm up overnight. 70 ml saturated sodium bicarbonate solution was added and after 30 minutes the two phases were extracted, and the aqueous phase was extracted twice with 150 mL DCM. The organic phase was dried over sodium sulphate and the solvent was removed under reduced pressure. The crude product was purified *via* column chromatography (dichloromethane : methanol; 90 : 10). RF(dichloromethane : methanol; 90 : 10) = 0.15. The product was isolated as brown powder (3.113 g, 12.10 mmol, 30%).^{1}H-NMR (400 MHz, chloroform-d δ(ppm)): 8.59–8.53 (m, 2H), 7.67 (td, J = 7.7, 1.8 Hz, 1H), 7.33–7.29 (m, 1H), 7.23 (ddd, J = 7.6, 4.9, 1.2 Hz, 1H), 4.11 (s, 2H), 3.61 (s, 1H).

1-(5-Phenyl-1,3,4-thiadiazol-2-yl)-*N*,*N*-bis(pyridin-2-ylmethyl) methanamine ($L^{Ph\text{-}TDA}$). Bis(pyridin-2-ylmethyl)glycine (3.00 g, 11.66 mmol, 1 eq.) was solved in 80 mL dichloromethane under nitrogen atmosphere and ice cooling. Carbonyldiimidazol (1.89, 11.66 mmol, 1eq.) was added to the solution and stirred for 1 h. Afterwards benzohydrazide (1.59, 11.66 mmol, 1eq.) added and the suspension was stirred overnight. The solvent was removed under reduced pressure and the residue was solved in 100 ml dry THF under nitrogen atmosphere. Lawesson's reagent (5.16 g, 12.76 mmol, 1.1 eq.) was added and the yellow solution was stirred under reflux overnight. The solvent was removed under reduced pressure. The residue was mixed with 300 mL DCM and 75 mL saturated bicarbonate solution and extracted. The organic phase was twice washed with 75 mL saturated bicarbonate solution, dried over sodium sulphate and the solvent was removed under reduced pressure. The crude product was purified *via* column chromatography (dichloromethane : methanol; 95 : 5). The product was isolated as brown powder (3.69 g, 9.87 mmol, 85%). RF (dichloromethane : methanol; 95 : 5) = 0.21. ^{1}H-NMR (400 MHz, chloroform-*d* δ(ppm)): 8.60 (ddd, J = 4.9, 1.9, 0.9 Hz, 2H), 8.00–7.95 (m, 2H), 7.71 (td, J = 7.7, 1.8 Hz, 2H), 7.55 (dt, J = 7.8, 1.1 Hz, 2H), 7.51–7.47 (m, 3H), 7.21 (ddd, J = 7.5, 4.9, 1.2 Hz, 2H), 4.23 (s, 2H), 3.98 (s, 4H). ^{13}C NMR (101 MHz, chloroform-*d* δ(ppm)): 170, 169, 158, 149, 137, 131, 130, 129, 128, 123.17, 122, 60, 53. FT-IR: $\tilde{\nu}$ (cm^{-1}) = 2935, 2820, 1587, 1567, 1474, 1456, 1431, 1358, 1309, 1240, 1181, 1143, 1110, 1085, 1064, 1043, 1026, 995, 975, 961, 914, 889, 875, 835, 773, 756, 684, 625, 608, 577, 519, 507, 402; ESI-MS (m/z): calc. for $[C_{22}H_{22}N_5S_1]^+$ expected: 374.14 (100.00%); found: 374.143 (100.00%); elemental analysis calculated for $L^{Ph\text{-}TDA}$ 0.4 DCM ($C_{23.4}H_{21.8}N_5SCl_{0.8}$): C, 63.54, H, 4.90, N, 16.45. Found: C, 63.83, H, 5.21, N, 16.62.

Complex synthesis

The precursor complex $[Fe(py)_4(NCS)_2]$, $[Fe(py)_4(NCSe)_2]$ and $[Fe(py)_4(NCBH_3)_2]$ were synthesised accordingly to literature known procedure.[14]

$[Fe(L^{Ph\text{-}TDA})(NCS)_2]$ (C1). The following reaction was carried out in a glovebox under an inert atmosphere. $[Fe(py)_4(NCS)_2]$ (231.0 mg, 0.3143 mmol, 1 eq.) was suspended in 16 mL dry acetonitrile and stirred for 30 minutes. The suspension was added to a solution of $L^{Ph\text{-}TDA}$ (174.5 mg, 0.4672 mmol, 1 eq.) in 2 mL of acetonitrile and the resulting orange mixture was stirred for 1 h. The reaction mixture was filtered and set for slow evaporation. Orange crystals suitable for X-ray diffraction were obtained after four days of slow evaporation directly from the mother liquor and the microcrystalline material was obtained by filtration in moderate yield (173 mg, 0.4672 mmol, 67%) was used for other bulk analysis. FT-IR: $\tilde{\nu}$ (cm^{-1}) 2914, 2047, 1600, 1570, 1459, 1432, 1348, 1307, 1250, 1148, 1097, 1048, 1017, 988, 954, 874, 823, 795, 762, 733, 688, 641, 511, 492, 471; ESI-MS (m/z): calc. for $[C_{22}H_{19}FeN_6S_2]^+$ expected: 487.05 (100.00%); found: 487.05 (100.00%); elemental analysis calculated for $[Fe(L^{Ph\text{-}TDA})(NCS)_2]\cdot H_2O$ ($C_{23}H_{21}FeN_7OS_3$): C, 49.21, H, 3.86, N, 17.15. Found: C, 49.03, H, 3.76, N, 17.40.

$[Fe(L^{Ph\text{-}TDA})(NCSe)_2]$ (C2). The following reaction was carried out in a glovebox under an inert atmosphere. $[Fe(py)_4(NCSe)_2]$ (231.0 mg, 0.4672 mmol, 1 eq.) was suspended in 16 mL dry acetonitrile and stirred for 30 minutes. The suspension was added to a solution of $L^{Ph\text{-}TDA}$ (174.5 mg, 0.4672 mmol, 1 eq.) in 2 mL of acetonitrile and the resulting yellow mixture was stirred for 1 h. The reaction mixture was filtered and set for slow evaporation. Yellow crystals suitable for X-ray diffraction were obtained after four days of slow evaporation directly from the mother liquor and the microcrystalline material was

obtained by filtration in moderate (179 mg, 0.2781 mmol, 60%), was used for other bulk analysis. FT-IR: $\tilde{\nu}$ (cm^{-1}) 2905, 2061, 1763, 1603, 1570, 1476, 1458, 1438, 1349, 1304, 1282, 1254, 1171, 1153, 1097, 1073, 1048, 1017, 998, 969, 955, 940, 896, 874, 823, 759, 732, 690, 640, 618, 581, 511, 496, 476, 447, 423; ESI-MS (m/z): calc. for $[C_{22}H_{19}FeN_6SSe]^+$ expected: 535.0 (100.00%); found: 535.0 (100%); elemental analysis calculated for $[Fe(\mathbf{L^{Ph\text{-}TDA}})(NCSe)_2]\cdot H_2O$ ($C_{23}H_{21}FeN_7O_1SSe_2$): C, 42.10, H, 3.28, N, 13.64. Found: C, 42.03, H, 3.22, N, 14.92.

$[Fe(\mathbf{L^{Ph\text{-}TDA}})(NCBH_3)_2]$ (C3). The following reaction was carried out in a glovebox under an inert atmosphere. $[Fe(py)_4(NCBH_3)_2]$ (107.0 mg, 0.2336 mmol, 1 eq.) was suspended in 8 mL dry acetonitrile and stirred for 30 minutes. The suspension was added to a solution of $\mathbf{L^{Ph\text{-}TDA}}$ (87.25 mg, 0.2336 mmol, 1 eq.) in 1 mL of acetonitrile and the resulting mixture was stirred for 1 h. The reaction mixture was filtered and set for slow evaporation. Brown crystals suitable for X-ray diffraction were obtained after four days of slow evaporation directly from the mother liquor and the microcrystalline material was obtained by filtration in moderate (29.75 mg, 0.05845 mmol, 25%), was used for other bulk analysis. FT-IR: $\tilde{\nu}$ (cm^{-1}) = 2916, 2338, 2182, 1626, 1604, 1571, 1479, 1460, 1441, 1351, 1316, 1287, 1252, 1115, 1050, 1020, 989, 956, 880, 805, 760, 733, 689, 642, 578, 511, 493, 454, 417; ESI-MS (m/z): calc. for $[C_{23}H_{24}BFeN_6S]^+$ expected: 469.11 (100.00%); found: 469.11 (100.00%); elemental analysis calculated for $[Fe(\mathbf{L^{Ph\text{-}TDA}})(NCBH_3)_2]\cdot H_2O$ ($C_{24}H_{29}B_2FeN_7OS$): C, 52.27, H, 4.91, N, 19.24. Found: C, 52.42, H, 5.16, N, 18.60.

Conflicts of interest

There are no conflicts to declare.

Data availability

All the raw data from this manuscript have been uploaded to Zenodo and are freely available *via* https://doi.org/10.5281/zenodo.17609511. All the processed data supporting the findings of this study can be found in the article and the supplementary information (SI). Supplementary information is available. See DOI: https://doi.org/10.1039/d5dt02912k.

CCDC 2480291–2480295 contain the supplementary crystallographic data for this paper.[61a–e]

Acknowledgements

The authors thank Dr Robert Naumann and Prof. Heinze (JGU) for the solid state UV-Vis measurements and evaluation of the data. JGB, JAW, VS and ER acknowledge funding from the Deutsche Forschungsgemeinschaft (DFG, German Research Foundation)-TRR 173-268565370 Spin+X (Project No. A04). J. A. W. and V. S. are grateful to Allianz für Hochleistungsrechnen Rheinland–Pfalz (AHRP) for providing CPU-time within the project RPTU-SPINPLUSXA4.

References

1 J. S. Miller, *Chem. Soc. Rev.*, 2011, **40**, 3266.
2 E. Collet, H. Watanabe, N. Bréfuel, L. Palatinus, L. Roudaut, L. Toupet, K. Tanaka, J.-P. Tuchagues, P. Fertey, S. Ravy, B. Toudic and H. Cailleau, *Phys. Rev. Lett.*, 2012, **109**, 257206.
3 S. Kamilya, S. Mehta, M. Semwal, R. Lescouëzec, Y. Li, J. Pechousek, V. R. Reddy, E. Rivière, M. Rouzières and A. Mondal, *Inorg. Chem.*, 2023, **62**, 8794–8802.
4 J. E. Clements, J. R. Price, S. M. Neville and C. J. Kepert, *Angew. Chem., Int. Ed.*, 2016, **55**, 15105–15109.
5 J. Cruddas and B. J. Powell, *J. Am. Chem. Soc.*, 2019, **141**, 19790–19799.
6 A. Rotaru, I. A. Gural'skiy, G. Molnár, L. Salmon, P. Demont and A. Bousseksou, *Chem. Commun.*, 2012, **48**, 4163–4165.
7 Z.-B. Hu, X. Yang, J. Zhang, L.-A. Gui, Y.-F. Zhang, X.-D. Liu, Z.-H. Zhou, Y. Jiang, Y. Zhang, S. Dong and Y. Song, *Nat. Commun.*, 2024, **15**, 4702.
8 Z. Zhang, C. Duan, S. Wang, T. Xie, F. Zou, Y. Luo, R. Tang, K. Guo, L. Yuan, K. Zhang, Y. Wang, J. Qiu and K. Yan, *Angew. Chem.*, 2024, **136**, e202412042.
9 Q. Li and Z. Li, *Acc. Chem. Res.*, 2020, **53**, 962–973.
10 J. J. Zakrzewski, M. Liberka, J. Wang, S. Chorazy and S. Ohkoshi, *Chem. Rev.*, 2024, **124**, 5930–6050.
11 P. Gütlich, A. Hauser and H. Spiering, *Angew. Chem., Int. Ed. Engl.*, 1994, **33**, 2024–2054.
12 P. Gutlich, V. Ksenofontov and A. Gaspar, *Coord. Chem. Rev.*, 2005, **249**, 1811–1829.
13 G. D. Harzmann, R. Frisenda, H. S. J. Van Der Zant and M. Mayor, *Angew. Chem., Int. Ed.*, 2015, **54**, 13425–13430.
14 R. G. T. Ramírez, E. Trzop and E. Collet, *Dalton Trans.*, 2024, **53**, 10159–10167.
15 G. Azzolina, R. Bertoni and E. Collet, *J. Appl. Phys.*, 2021, **129**, 085106.
16 M. Shatruk, H. Phan, B. A. Chrisostomo and A. Suleimenova, *Coord. Chem. Rev.*, 2015, **289–290**, 62–73.
17 A.-I. Popa, L. Stoleriu and C. Enachescu, *J. Appl. Phys.*, 2021, **129**, 131101.
18 M. Nishino, Y. Singh, K. Boukheddaden and S. Miyashita, *J. Appl. Phys.*, 2021, **130**, 141102.
19 E. Collet and G. Azzolina, *Phys. Rev. Mater.*, 2021, **5**, 044401.
20 J. Pavlik and R. Boča, *Eur. J. Inorg. Chem.*, 2013, **2013**, 697–709.
21 K. D. Murnaghan, C. Carbonera, L. Toupet, M. Griffin, M. M. Dîrtu, C. Desplanches, Y. Garcia, E. Collet, J. Létard and G. G. Morgan, *Chem. – Eur. J.*, 2014, **20**, 5613–5618.
22 Y. Garcia, O. Kahn, L. Rabardel, B. Chansou, L. Salmon and J. P. Tuchagues, *Inorg. Chem.*, 1999, **38**, 4663–4670.
23 E. Milin, V. Patinec, S. Triki, E.-E. Bendeif, S. Pillet, M. Marchivie, G. Chastanet and K. Boukheddaden, *Inorg. Chem.*, 2016, **55**, 11652–11661.
24 T. Boonprab, S. J. Lee, S. G. Telfer, K. S. Murray, W. Phonsri, G. Chastanet, E. Collet, E. Trzop,

G. N. L. Jameson, P. Harding and D. J. Harding, *Angew. Chem.*, 2019, **131**, 11937–11941.
25 G. Li, O. Stefanczyk, K. Kumar, L. Guérin, K. Okuzono, K. Tran, M. S. Kilic, K. Nakabayashi, K. Imoto, A. Namai, Y. Nakamura, S. R. Maity, F. Renz, G. Chastanet and S. Ohkoshi, *Angew. Chem., Int. Ed.*, 2025, **64**, e202423095.
26 J. Kiehl, T. Hochdörffer, L. M. Carrella, V. Schünemann, M. H. Nygaard, J. Overgaard and E. Rentschler, *Inorg. Chem.*, 2022, **61**, 3141–3151.
27 C. Köhler and E. Rentschler, *Eur. J. Inorg. Chem.*, 2016, **2016**, 1955–1960.
28 S. Sundaresan, J.-G. Becker, J. Eppelsheimer, A. E. Sedykh, L. M. Carrella, K. Müller-Buschbaum and E. Rentschler, *Dalton Trans.*, 2023, **52**, 13181–13189.
29 P. Gütlich, Y. Garcia and H. A. Goodwin, *Chem. Soc. Rev.*, 2000, **29**, 419–427.
30 D. J. Harding, P. Harding and W. Phonsri, *Coord. Chem. Rev.*, 2016, **313**, 38–61.
31 M. You, G. T. Nguyen, D. Shao, T. Wang, X.-Y. Chang, L. Ungur and Y.-Z. Zhang, *Dalton Trans.*, 2022, **51**, 5596–5602.
32 S. Sundaresan and S. Brooker, *Inorg. Chem.*, 2023, **62**, 12192–12202.
33 S. Sundaresan, J. Eppelsheimer, E. Gera, L. Wiener, L. M. Carrella, K. R. Vignesh and E. Rentschler, *Dalton Trans.*, 2024, **53**, 10303–10317.
34 R. W. Hogue, R. G. Miller, N. G. White, H. L. C. Feltham, G. N. L. Jameson and S. Brooker, *Chem. Commun.*, 2014, **50**, 1435–1437.
35 A. Arroyave, A. Lennartson, A. Dragulescu-Andrasi, K. S. Pedersen, S. Piligkos, S. A. Stoian, S. M. Greer, C. Pak, O. Hietsoi, H. Phan, S. Hill, C. J. McKenzie and M. Shatruk, *Inorg. Chem.*, 2016, **55**, 5904–5913.
36 J.-G. Becker, S. Sundaresan, L. M. Carrella and E. Rentschler, *Chem. Commun.*, 2025, **61**, 13389–13392.
37 P. N. Basa, C. A. Barr, K. M. Oakley, X. Liang and S. C. Burdette, *J. Am. Chem. Soc.*, 2019, **141**, 12100–12108.
38 S. K. Levadala, S. R. Banerjee, K. P. Maresca, J. W. Babich and J. Zubieta, *Synthesis*, 2004, **11**, 1759–1766.
39 A. A. Pund, S. S. Saboo, G. M. Sonawane, A. C. Dukale and B. K. Magare, *Synth. Commun.*, 2020, **50**, 3854–3864.
40 A. A. Pund, M. H. Shaikh, B. G. Chandak, V. N. Bhosale and B. K. Magare, *Polycyclic Aromat. Compd.*, 2023, **43**, 1247–1262.
41 G. Nagendra, R. S. Lamani, N. Narendra and V. V. Sureshbabu, *Tetrahedron Lett.*, 2010, **51**, 6338–6341.
42 H. S. Scott, R. W. Staniland and P. E. Kruger, *Coord. Chem. Rev.*, 2018, **362**, 24–43.
43 S. Yuan, N. Natt and B. J. Powell, *Inorg. Chem.*, 2025, **64**, 7182–7193.
44 A. Kálmán, G. Argay, D. Scharfenberg-Pfeiffer, E. Höhne and B. Ribár, *Acta Crystallogr., Sect. B: Struct. Sci.*, 1991, **47**, 68–77.
45 S. Ranjan, R. Devarapalli, S. Kundu, S. Saha, S. Deolka, V. R. Vangala and C. M. Reddy, *IUCrJ*, 2020, **7**, 173–183.
46 P. Guionneau, *Dalton Trans.*, 2014, **43**, 382–393.
47 E. Kuzmann, Z. Homonnay, Z. Klencsár and R. Szalay, *Molecules*, 2021, **26**, 1062.
48 J. A. Wolny, K. Gröpl, J. Kiehl, E. Rentschler and V. Schünemann, *Dalton Trans.*, 2024, **53**, 8391–8397.
49 J. A. Wolny, X. Li, M. Dîrtu, K. Gröpl, T. Hochdörffer, H. Paulsen, Y. Garcia and V. Schünemann, *RSC Adv.*, 2025, **15**, 32009–32030.
50 J. C. Cobas and F. J. Sardina, *Concepts Magn. Reson., Part A*, 2003, **19**, 80–96.
51 G. M. Sheldrick, *Acta Crystallogr., Sect. A: Found. Adv.*, 2015, **71**, 3–8.
52 G. M. Sheldrick, *Acta Crystallogr., Sect. A: Found. Crystallogr.*, 2008, **64**, 112–122.
53 G. M. Sheldrick and T. R. Schneider, in *Methods in Enzymology*, Elsevier, 1997, pp. 319–343.
54 H. P. Gunnlaugsson, *Hyperfine Interact.*, 2016, **237**, 79.
55 M. J. Frisch, G. W. Trucks, H. B. Schlegel, G. E. Scuseria, M. A. Robb, J. R. Cheeseman, G. Scalmani, V. Barone, G. A. Petersson, H. Nakatsuji, X. Li, M. Caricato, A. V. Marenich, J. Bloino, B. G. Janesko, R. Gomperts, B. Mennucci, H. P. Hratchian, J. V. Ortiz, A. F. Izmaylov, J. L. Sonnenberg, D. Williams-Young, F. Ding, F. Lipparini, F. Egidi, J. Goings, B. Peng, A. Petrone, T. Henderson, D. Ranasinghe, V. G. Zakrzewski, J. Gao, N. Rega, G. Zheng, W. Liang, M. Hada, M. Ehara, K. Toyota, R. Fukuda, J. Hasegawa, M. Ishida, T. Nakajima, Y. Honda, O. Kitao, H. Nakai, T. Vreven, K. Throssell, J. A. Montgomery Jr., J. E. Peralta, F. Ogliaro, M. J. Bearpark, J. J. Heyd, E. N. Brothers, K. N. Kudin, V. N. Staroverov, T. A. Keith, R. Kobayashi, J. Normand, K. Raghavachari, A. P. Rendell, J. C. Burant, S. S. Iyengar, J. Tomasi, M. Cossi, J. M. Millam, M. Klene, C. Adamo, R. Cammi, J. W. Ochterski, R. L. Martin, K. Morokuma, O. Farkas, J. B. Foresman and D. J. Fox, *Gaussian 16, Revision A.03*, 2016.
56 T. Yanai, D. P. Tew and N. C. Handy, *Chem. Phys. Lett.*, 2004, **393**, 51–57.
57 W. J. Stevens, H. Basch and M. Krauss, *J. Chem. Phys.*, 1984, **81**, 6026–6033.
58 W. J. Stevens, M. Krauss, H. Basch and P. G. Jasien, *Can. J. Chem.*, 1992, **70**, 612–630.
59 T. R. Cundari and W. J. Stevens, *J. Chem. Phys.*, 1993, **98**, 5555–5565.
60 S. Grimme, J. Antony, S. Ehrlich and H. Krieg, *J. Chem. Phys.*, 2010, **132**, 154104.
61 (*a*) CCDC 2480291: Experimental Crystal Structure Determination, 2026, DOI: 10.5517/ccdc.csd.cc2p7yd9; (*b*) CCDC 2480292: Experimental Crystal Structure Determination, 2026, DOI: 10.5517/ccdc.csd.cc2p7yfb; (*c*) CCDC 2480293: Experimental Crystal Structure Determination, 2026, DOI: 10.5517/ccdc.csd.cc2p7ygc; (*d*) CCDC 2480294: Experimental Crystal Structure Determination, 2026, DOI: 10.5517/ccdc.csd.cc2p7yhd; (*e*) CCDC 2480295: Experimental Crystal Structure Determination, 2026, DOI: 10.5517/ccdc.csd.cc2p7yjf.